

# Relating the formation energies for oxygen vacancy defects to the structural properties of tungsten oxides

Ryan Kerr<sup>a</sup>, Mark R. Gilbert<sup>b</sup>, Samuel T. Murphy<sup>a,\*</sup>

<sup>a</sup>*Engineering Department, Lancaster University, Bailrigg, Lancashire, LA1 4YW, UK*

<sup>b</sup>*United Kingdom Atomic Energy Authority, Culham Centre for Fusion Energy, Culham Science Centre, Abingdon, Oxon, OX14 3DB, UK*

---

## Abstract

Tungsten is one of the materials of choice for several commercial fusion power plant designs, in particular, for divertor targets and the first wall. In maintenance conditions or during a loss of coolant accident, tungsten is expected to reach temperatures at which it readily volatilises as tungsten trioxide, potentially distributing radioactive material and posing a hazard to personnel. The oxidation of tungsten is reported to show an orientation dependence, however, the mechanism by which it occurs is not fully understood, providing an obstacle to the development of tungsten smart alloys that display reduced oxidation. Using DFT+ $U$  simulations, it is shown how key features of the electronic structure of the tungsten-oxygen system change as the tungsten-oxygen ratio evolves. Formation and migration barriers for oxygen in the different tungsten oxides are determined, allowing an assessment of its mobility in the phases observed during the oxidation process. Our results provide a new level of understanding of the sub-stoichiometric Magnéli phases that are observed during the oxidation of tungsten, which are perceived to be composed of  $WO_2$ - and  $WO_3$ -like regions.

*Keywords:* tungsten,  $WO_3$ , DFT, vacancy

---

\*Corresponding author

*Email address:* `samuel.murphy@lancaster.ac.uk` (Samuel T. Murphy)

## 1. Introduction

Tungsten is a candidate material for use in the first wall and divertor targets of several proposed tokamak fusion devices, including the United Kingdom's STEP project, owing to its favourable thermal and physical properties [1]. However, theoretical studies have shown that pure tungsten first walls may reach temperatures of over 1300 K in the event of a loss of coolant accident [2]. The primary cause of this temperature rise is the decay heat produced by activated tungsten and its decay products, particularly the decay of  $^{187}\text{W}$ , formed via neutron capture by  $^{186}\text{W}$  [3]. At these temperatures, tungsten is known to readily oxidise in the presence of air to form tungsten trioxide,  $\text{WO}_3$ , which begins at temperatures of around 1000 K [4]. The rapid oxidation of irradiated tungsten enables the mobilisation of both tritium and the activation products of tungsten due to surface volatilisation, posing a safety hazard to first-responders and other on-site personnel [2]. Similar conditions may be encountered during maintenance activities and decommissioning, thereby requiring strict atmospheric control. Alternatively, a deeper understanding of how and why tungsten oxides form is key to guiding materials choices and the development of new, radiation- and oxidation-resistant materials for use in future reactor designs.

The oxidation of tungsten has been widely studied over recent decades, but no firm consensus exists as to the mechanism by which it is oxidised to tungsten trioxide,  $\text{WO}_3$ . It is known to exhibit a strong dependence on oxidation conditions and grain orientation, and to proceed through a series of tungsten oxides as oxygen content in the system increases [5]. This process is well-summarised in the work of Cifuentes *et al.*: at around 600°C,  $\text{W}_{18}\text{O}_{49}$  ( $\text{WO}_{2.72}$ ) forms a protective oxide-metal interface, which cracks as it reaches a critical thickness. Subsequent ingress of oxygen through these cracks leads to the formation of columnar  $\text{W}_{25}\text{O}_{73}$  ( $\text{WO}_{2.92}$ ), leading to rapid growth of the oxide scale, followed by eventual transformation into  $\text{WO}_3$  as the oxygen concentration at the interface grows [6]. Under the Wagner theory of oxidation, the growth of the oxide layer is controlled by the rate of ion transport and is dependent on the

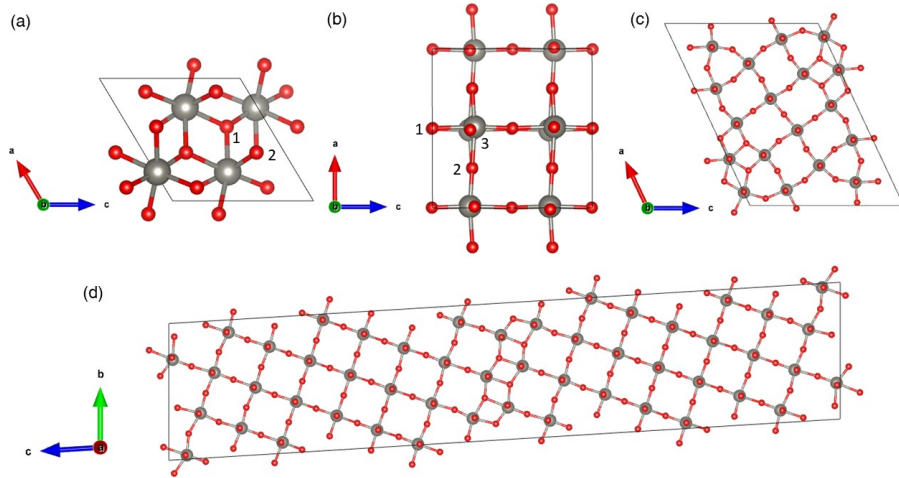


Figure 1: Crystal structures of (a)  $\text{WO}_2$ , (b)  $\text{WO}_3$ , (c)  $\text{W}_{18}\text{O}_{49}$  ( $\text{WO}_{2.72}$ ) and (d)  $\text{W}_{25}\text{O}_{73}$  ( $\text{WO}_{2.92}$ ). Grey atoms denote tungsten. Red atoms denote oxygen. Unique Oxygen sites in  $\text{WO}_2$  and  $\text{WO}_3$  are denoted by the numbers 1-2 and 1-3, respectively.

concentration gradients through the oxide scale [7]. As such, in this work, we consider the role of oxygen vacancies as the means of establishing a concentration gradient in the oxide phases of interest, which are discussed below.

### 1.1. Crystallography

35 This brief summary highlights the key tungsten oxide phases. A description of each is provided below and illustrations are presented in Figure 1:

- a) Tungsten trioxide exhibits a range of polymorphs in the temperature range of  $0 < T < 1000$  K: monoclinic,  $< 223$  K; triclinic,  $223 - 288$  K; monoclinic,  $288 - 603$  K; orthorhombic,  $603 - 1013$  K; tetragonal,  $> 1013$  K. The room temperature monoclinic phase with the space group  $\text{P}2_1/c$  is studied in this work. This phase includes three unique oxygen sites at the  $4e$  Wyckoff positions, each bonded to two equivalent  $\text{W}^{6+}$  ions also at  $4e$  Wyckoff positions [8, 9].
- 40
- b) Tungsten dioxide,  $\text{WO}_2$ , is observed at lower temperatures and oxygen

45 partial pressures. The most stable phase of  $\text{WO}_2$  crystallises in the monoclinic  $\text{P}2_1/c$  space group. One  $\text{W}^{4+}$  ion occupies a  $4e$  Wyckoff position, whilst two oxygen ions occupy inequivalent  $4e$  Wyckoff positions [10, 11, 12].

c) The  $\text{W}_{18}\text{O}_{49}$  phase (alternatively  $\text{WO}_{2.72}$ ), which exhibits a tungsten  
50 bronze-like structure in the monoclinic  $\text{P}2/m$  space group, with a  $\beta$  angle of  $115.20^\circ$  according to Salje *et al.* This phase consists of 16 oxygen ions at  $2n$  Wyckoff positions, 9 at  $2m$  Wyckoff positions, and 1 oxygen ion at the  $1f$  Wyckoff position. The tungsten ions, in a 10:8 mixture of  $\text{W}^{5+}$  and  $\text{W}^{6+}$  oxidation states, occupy the  $2n$  Wyckoff positions [13, 14].

55 d) The  $\text{W}_{25}\text{O}_{73}$  phase (alternatively  $\text{WO}_{2.92}$ ) exhibits a sheer structure of the monoclinic  $\text{P}2/c$  space group with a  $\beta$  angle of  $98.3^\circ$ . This phase consists of 37 unique oxygen sites, 1 at the  $2f$  Wyckoff positions and the remaining at the  $4g$  Wyckoff positions. The tungsten ions occupy 13 unique sites, one at the  $2f$  Wyckoff position and the remainder at the  $4g$  Wyckoff positions,  
60 in a 1:12 mixture of  $\text{W}^{5+}$  and  $\text{W}^{6+}$  oxidation states [15].

In this work, we examine the thermodynamics and kinetics for oxygen transport, mediated via vacancies, through the tungsten oxide phases  $\text{WO}_2$ ,  $\text{WO}_3$ , and the so-called 'Magnéli' phases  $\text{W}_{18}\text{O}_{49}$  and  $\text{W}_{25}\text{O}_{73}$  to better understand the oxidation process. To support our discussion we provide a detailed review  
65 of the physical structure of each phase and investigation into the evolution of their electronic structures with increasing oxygen content.

## 2. Methodology

### 2.1. Density Functional Theory

All calculations herein were performed at the DFT level of theory as implemented in the VASP package [16, 17, 18, 19]. Standard PAW pseudopotentials  
70 were used with 14 valence electrons for W, treating the  $5s$ ,  $6s$ ,  $5p$  and  $5d$  electrons as valence, and six electrons for O, treating the  $2s$  and  $2p$  orbitals as va-

lence. A plane-wave cut-off energy of 520 eV was selected based on convergence testing and a Monkhorst-Pack  $k$ -point mesh was optimised for each structure.

75 In all cases, the  $k$ -point grids were converged to ensure a tolerance of 1 meV per atom. For unit cells, the dimensions of the Monkhorst-Pack grids were:  $\text{WO}_3$ ,  $6 \times 6 \times 6$ ;  $\text{WO}_2$ ,  $8 \times 8 \times 8$ ;  $\text{W}_{18}\text{O}_{49}$ ,  $1 \times 4 \times 1$ ;  $\text{W}_{25}\text{O}_{73}$ ,  $6 \times 1 \times 1$ . Gaussian smearing with a smearing width of 0.2 eV was applied to the electronic bands. In ionic relaxation, the ionic positions, cell volume and shape were relaxed until

80 the maximum force exerted on any atom in a single dimension met the criterion  $|\mathbf{F}| < 1 \text{ meV}/\text{\AA}$ . All calculations were performed spin-polarised; the magnetic moments were relaxed during the energy minimisation process and were initially set to  $\pm 5.0 \mu\text{B}$  as necessary to test both ferromagnetic, antiferromagnetic and non-magnetic configurations.

In order to account for on-site Coulombic interactions between localised W  $5d$  electrons, all calculations were performed under the rotationally invariant DFT+ $U$  formalism as described by Dudarev *et al.*, i.e.,  $U_{eff} = U - J$  [20]. In this work,  $J = 0$ , and hence  $U_{eff} = U$ , which was calculated *ab initio* under the linear response ansatz described by Cococcioni *et al.* [21]. For a singular W atom, a small change is made in the  $U$  parameter,  $V$ , ranging from  $V = -0.25 \text{ eV}$  to  $0.25 \text{ eV}$  in steps of  $0.05 \text{ eV}$ . At each step, the occupancy of the W  $5d$  orbitals of the atom is computed in both the self-consistent and non-self-consistent fields. The W  $5d$  occupancies are then plotted against  $V$ , and the  $U$  parameter is calculated as:

$$U = \chi^{-1} - \chi_0^{-1} \approx \left( \frac{\partial N_I^{SCF}}{\partial V_I} \right)^{-1} - \left( \frac{\partial N_I^{NSCF}}{\partial V_I} \right)^{-1} \quad (1)$$

85 where,  $N_I^{SCF}$  and  $N_I^{NSCF}$  is the number of electrons occupying the  $d$  orbital of the W atom to which  $V$  is applied in the self-consistent field and non-self-consistent field settings respectively. As such, the  $U$  parameters used in this work are:  $\text{WO}_3$ , 5.13 eV;  $\text{WO}_2$ , 4.13 eV;  $\text{W}_{18}\text{O}_{49}$ , 4.23 eV;  $\text{W}_{25}\text{O}_{73}$ , 3.75 eV.

## 2.2. Defect Formalism

The formation energy of the oxygen vacancies in the tungsten oxide phases was calculated according to equation 2:

$$\Delta E_f^i = E_{\text{defect}} - E_{\text{perfect}} + \mu_O + q(E_{\text{VBM}} + \varepsilon_f) + E_{\text{corr}} \quad (2)$$

where,  $E_{\text{perfect}}$  is the DFT energy of the perfect system,  $E_{\text{defect}}$  is the DFT energy of the system with one oxygen vacancy,  $\mu_O$  is the chemical potential of oxygen,  $q$  is the charge of the vacancy (in non-metallic systems),  $E_{\text{VBM}}$  and  $\varepsilon_f$  are the energies of the valance band maximum and Fermi level respectively, and  $E_{\text{corr}}$  is the Kumagai charge correction term to account for the finite size of the simulation supercell [22]. Since  $\text{WO}_3$  is non-metallic, and its defects may exhibit multiple charge states, its dielectric tensor for  $\text{WO}_3$  was calculated *ab initio*, using density functional perturbation theory (DFPT) as implemented in VASP. The dielectric tensors for all other phases were not required, as the charge correction factor reduces to zero for uncharged systems. For  $\text{WO}_3$ , the calculated dielectric tensor (equation 3) was predicted to be roughly isotropic.

$$\epsilon = \begin{bmatrix} 57.02 & 0.01 & -0.07 \\ -1.02 & 58.06 & -1.02 \\ -0.07 & 0.01 & 54.77 \end{bmatrix} \quad (3)$$

90 Calculation of defect formation energies was performed in supercells, however, the exact size of the supercell depended on the system of interest. For  $\text{WO}_3$  and  $\text{WO}_2$  supercells were constructed from  $3 \times 3 \times 3$  replications of unit cells, whilst for  $\text{W}_{18}\text{O}_{49}$  and  $\text{W}_{25}\text{O}_{73}$  supercells were constructed from  $1 \times 2 \times 1$  repetitions of the unit cells. During optimisation of the defect-containing supercells, the lattice parameters remained fixed to best mimic an isolated defect.  
95 While for the examination of the crystal structures we present results using a range of functionals, only the Generalised Gradient Approximation (GGA) unctional of Perdew *et al.* is used for the defect simulations [23].

The chemical potential of oxygen was defined at two limits. Under the oxygen-rich condition,  $\mu_O^{O\text{-rich}}$  was determined from a DFT simulation of the  
100

oxygen dimer in an arbitrarily large ( $a = b = c = 10 \text{ \AA}$ ) unit cell, whose dimensions were constrained during the calculation. The O-O bond length was then optimised and the energy of the system was extracted and halved to find  $\mu_{\text{O}} = -4.94 \text{ eV}$  with a bond length of  $1.211 \text{ \AA}$  (compared to  $1.207 \text{ \AA}$  experimentally).  
 105 In the oxygen-poor limit, the chemical potential was determined according to:

$$\mu_{\text{O}}^{O\text{-poor}} = \frac{\mu_{\text{W}_y\text{O}_x} - y\mu_{\text{W}_{(s)}}}{x} \quad (4)$$

where,  $\mu_{\text{WO}_2}$  and  $\mu_{\text{W}_{(s)}}$  are the chemical potentials of the tungsten oxide and tungsten metal respectively. The chemical potential of W was taken as the DFT energy of a single atom in bcc W,  $\mu_{\text{W}_{(s)}} = -12.98 \text{ eV}$ .

### 2.3. Activation Energies

110 Activation barriers to diffusion have been calculated using the climbing image nudged elastic band code provided by the VASP Transition State Tools package [24]. In the case of  $\text{WO}_3$  we calculate the migration energy for the oxygen vacancy in +2, +1 and 0 charge states.

## 3. Results and Discussion

### 115 3.1. Crystal Structure

For each phase of interest, the lattice parameters, cell angles and band gaps calculated using different exchange-correlation functionals are presented in Table 1. Local and semi-local exchange-correlation functionals, such as the Local Density Approximation (LDA) and the Generalized Gradient Approximation  
 120 functionals, are known to underestimate the band gap,  $E_g$ , while hybrid functionals such as that of Heyd, Scuseria and Ernzerhof (HSE06) are expected to give much more accurate values [34]. However, the use of hybrid functionals is prohibitively costly for studying the large number of defect formation energies required in this work. Further, there are known issues with the application of  
 125 hybrid functionals to metallic materials [35]. Therefore, in this work, the HSE06 functional was only used to examine  $\text{WO}_3$ .

XC Functional	U /eV	Lattice Parameters / Å			$\beta/^\circ$	Vol /Å <sup>3</sup>	E <sub>g</sub> /eV	Ref
		a	b	c				
WO <sub>3</sub>								
LDA *	5.13	7.61	7.61	7.63	90.01	441.87	0.79	-
PBE *	5.13	7.71	7.68	7.74	90.09	458.30	1.34	-
HSE06 *	NA	7.53	7.62	7.69	90.77	445.76	2.53	-
HSE06	NA	7.39	7.64	7.75	90.3	440.43	2.80	[25]
PBE	5.20	7.72	7.68	7.75	91.50	459.49	-	[26]
PBE	0.00	7.69	7.7	7.56	Unknown	Unknown	1.02	[27]
PBE	0.00	7.48	7.66	7.85	90.4	Unknown	~1	[28]
PW91	0.00	7.56	7.80	7.84	90.1	462.00	1.36	[29]
Tanisaki <i>et al.</i>	-	7.30	7.53	7.68	90.54	422.16	-	[30]
Saenz <i>et al.</i>	-	7.30	7.54	7.69	90.91	423.27	-	[31]
Loopstra <i>et al.</i>	-	7.31	7.54	7.69	90.9	423.85	2.6~3.2	[32]
WO <sub>2</sub>								
LDA *	4.84	5.52	4.89	5.64	120.42	152.24	-	-
PBE *	4.84	5.61	4.95	5.72	120.93	165.99	-	-
PBE	0.00	5.82	4.96	5.75	120.48	156.44	-	[10]
PBE	5.20	5.62	4.95	5.72	120.93	159.12	-	[26]
Bolzan <i>et al.</i>	-	5.57	4.90	5.66	120.68	154.48	-	[33]
W <sub>18</sub> O <sub>49</sub>								
PBE *	4.13	18.32	3.78	14.03	115.21	971.57	-	-
PBE	5.20	18.29	3.86	14.20	109.71	1008.87	-	[26]
Salje <i>et al.</i>	-	18.33	3.79	14.04	115.20	995.41	-	[14]
W <sub>25</sub> O <sub>73</sub>								
PBE *	3.75	12.12	3.86	59.83	93.51	2799.03	-	-
PBE	5.20	12.26	3.86	60.57	97.91	2866.39	-	[26]
Sundberg <i>et al.</i>	-	11.93	3.82	59.72	98.3	2721.60	-	[15]

Table 1: Lattice parameters and band gaps, E<sub>g</sub>, where applicable, for WO<sub>3</sub>, WO<sub>2</sub>, W<sub>18</sub>O<sub>49</sub> and W<sub>25</sub>O<sub>73</sub>. Asterisks (\*) denote parameters, cell volumes and band gaps calculated in this work. Experimental values are indicated with a *U* parameter of '-', whereas DFT studies which have not applied a *U* parameter are listed as *U* = 0. Similarly, studies where a band gap has not been evaluated are marked with a '-'.  
8

Table 2: Optimised bond lengths in  $\text{WO}_3$ . The number of the oxygen atom in the W-O bond is given in Figure 2a.

XC Functional	W-O <sub>x</sub> Bond Length / Å					
	1	2	3	4	5	6
LDA	1.93	1.88	1.90	1.91	1.95	1.86
PBE	1.87	2.00	1.96	1.90	1.85	2.03
HSE06	1.81	2.00	2.01	1.82	1.76	2.16

Table 3: Optimised bond lengths in  $\text{WO}_2$ . The number of the oxygen atom in the W-O bond is given in Figure 2b

XC Functional	W-O <sub>x</sub> Bond Length / Å					
	1	2	3	4	5	6
LDA	2.06	2.06	2.00	2.00	2.00	1.95
PBE	2.07	2.05	2.09	2.11	2.03	2.01

For room-temperature monoclinic  $\text{WO}_3$ , the results presented in Table 1 show that the DFT simulations performed here overestimate the lattice parameters, irrespective of the functional used, and is particularly marked for the semi-local functionals. As also highlighted in Table 1, this overestimation has been observed in a number of studies using different functionals, codes and parameterisations. While it is true that the PBE typically overestimates lattice parameters and the LDA underestimates them, here both overestimate the volume for  $\text{WO}_3$ . It is clear that the employment of the hybrid functional, which offers a better description of the correlated  $\text{WO}_3$ , does somewhat ameliorate the problem, however, there is still evidence of some overestimation of the lattice parameter, further, the  $U$ -parameter appears to have little impact.

Upon examination of individual W-O bond lengths within one  $\text{WO}_6$  octahedra, it can be seen that the average bond length in  $\text{WO}_3$  is around 1.94 Å when optimised using the PBE exchange-correlation functional. As shown in Table 2, there is a considerable distortion in the  $a$ -axis when optimised using the PBE functional. The deviation in our calculated structural parameters may be due

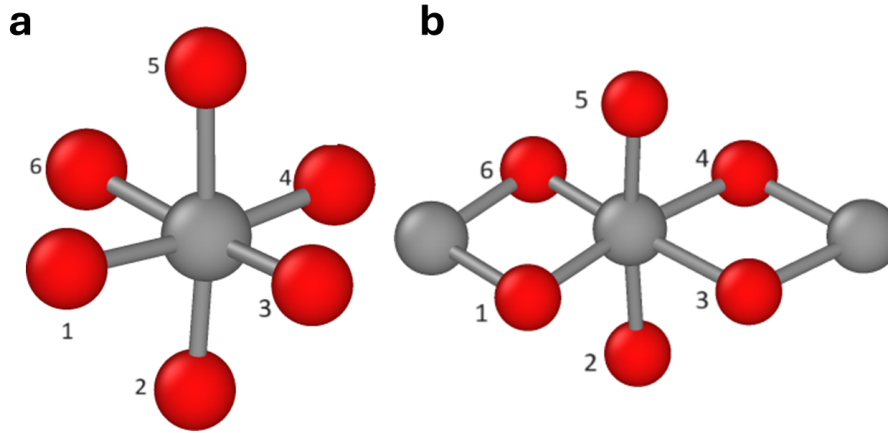


Figure 2: The numerical labels assigned to oxygen atoms in (a)  $\text{WO}_3$  and (b)  $\text{WO}_2$  for discussion of  $\text{W-O}_x$  bond lengths. The labels 1-2 for  $\text{WO}_2$  and 1-3 for  $\text{WO}_3$  also correspond to the unique oxygen sites highlighted in Figure 1.

to the initial structure employed in these calculations, which were available on the Inorganic Crystal Structural Database. There is a degree of uncertainty in  
 145 the positions of oxygen ions introduced by the Rietveld refinement of neutron powder refraction and X-ray diffraction experiments [36, 37, 38]. Combined with the close similarities in structure between the various tungsten trioxide phases, there is an increased likelihood of the structure relaxing into a local DFT minima.

150 A similar discrepancy with experimental data was observed for monoclinic  $\text{WO}_2$  using the PBE functional, particularly in the  $a$ - and  $c$ -axes. However, our results are in-line with previous DFT studies on the same phase [26, 10]. In addition, the average bond length in  $\text{WO}_2$  optimised using the PBE exchange-correlation functional is 2.08 Å. This is considerably higher than the average  
 155 bond length in  $\text{WO}_3$ . However, there is much more distortion in the bond lengths in  $\text{WO}_2$  when optimised using the PBE functional compared to the LDA functional.

$\text{W}_{25}\text{O}_{73}$  and  $\text{W}_{18}\text{O}_{49}$  were optimised using only the PBE exchange-correlation

functional. The lattice parameters obtained for these phases are much closer  
 160 to the experimentally observed values, although the computed values in the  $a$ -  
 and  $c$ -axes for  $W_{25}O_{73}$  are slightly larger. Upon examination of the structure of  
 $W_{25}O_{73}$ , the overestimation of the lattice parameters in the  $a$ - and  $c$ -axes may  
 be attributed to the similarity in geometry between this phase and  $WO_3$ , as the  
 former contains large regions of corner-sharing  $WO_6$  octahedra whilst the latter  
 165 consists solely of the same octahedral motifs.

### 3.2. Electronic Structure

The projected density of states (PDOS) for each phase of interest was ob-  
 tained using the PBE functional with the DFT+ $U$  formalism. Figure 3 shows  
 the gradual evolution of the total density of states with increasing oxygen con-  
 170 tent, from  $WO_2$  through to  $WO_3$ . The PDOS of the W  $5d$  and O  $2p$  states are  
 shown in blue and red respectively, and each plot is shifted such that the Fermi  
 level is at zero.  $WO_2$ ,  $W_{18}O_{49}$  and  $W_{25}O_{73}$  are all predicted to be metallic,  
 with their Fermi levels lying within bands exhibiting primarily W  $5d$  character.  
 Experimentally,  $W_{18}O_{49}$  is shown to possess semiconductor properties due to  
 175 its surface being covered with oxygen atoms, however, bulk  $W_{18}O_{49}$  is metallic  
 [39]. In  $WO_2$ , there is a band of W  $5d$  states just below the Fermi level; as  
 the oxygen content of the system increases, this band increases in energy and  
 eventually forms the conduction band seen in the DOS of  $WO_3$ . The Magnéli  
 phases exhibit features from the DOS of both  $WO_2$  and  $WO_3$ , and the band  
 180 gap exhibited in  $WO_3$  can first be seen in the DOS of  $W_{18}O_{49}$ , although the  
 Fermi level is still within the band.

The magnetic moments of each atom in each phase were allowed to relax  
 to their lowest-energy configurations. In  $WO_2$ , ferromagnetic ordering was pre-  
 dicted with magnetic moments of approximately  $+0.890 \mu_B$  on each W atom.  
 185 In  $W_{18}O_{49}$ , ferromagnetic ordering was predicted with magnetic moments rang-  
 ing from  $+0.146$  to  $+0.494 \mu_B$  on each W atom. The distribution of magnetic  
 moments is shown in Figure 4. In  $W_{25}O_{73}$ , a total magnetic moment of  $+0.005$   
 $\mu_B$  was predicted, indicating negligible magnetic ordering. Finally, in  $WO_3$ , the

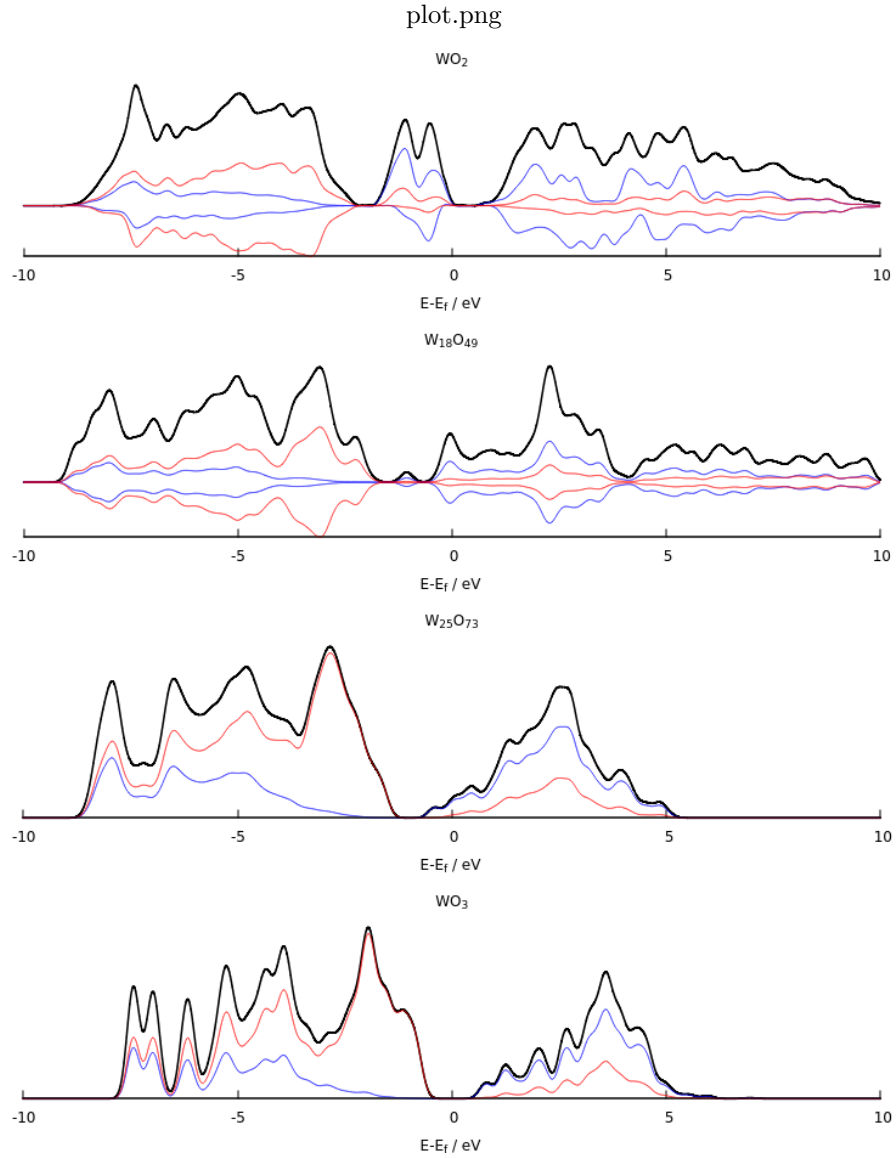


Figure 3: Projected and total density of states of the tungsten oxide phases investigated in this study. The Fermi level was set to zero. The black line represents the total density of states and the red and blue lines represent the projected DoS for the O  $2p$  and W  $5d$  orbitals respectively.

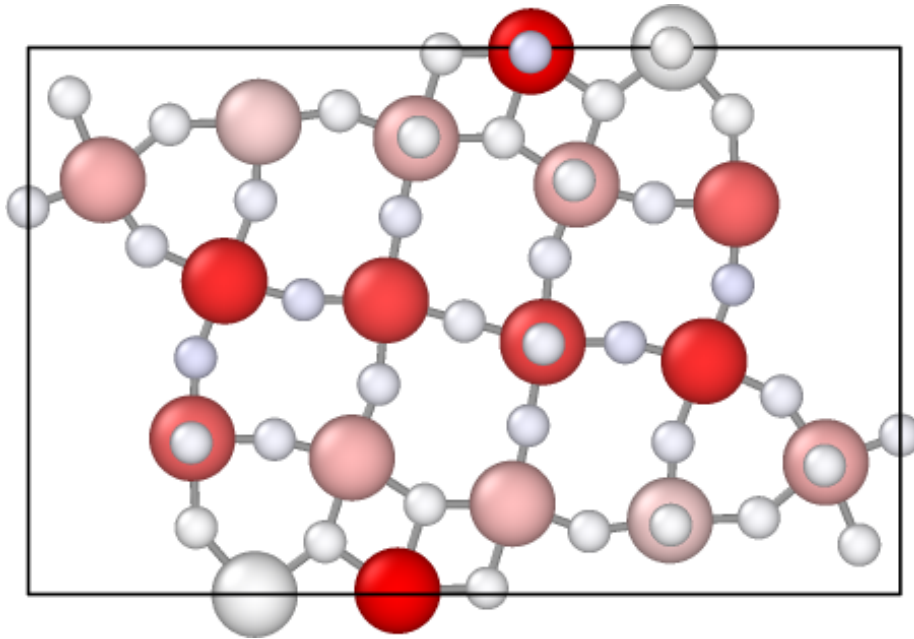


Figure 4: Distribution of magnetic moments in  $W_{18}O_{49}$ , ranging from  $0.000 \mu_B$  (white) to  $+0.494 \mu_B$  (red).

ground state configuration in these calculations was non-magnetic. It is known  
 190 experimentally that  $WO_3$  is paramagnetic, however, due to the limitations of  
 the DFT method, the paramagnetic ordering in  $WO_3$  cannot be accurately  
 represented, and therefore the non-magnetic configuration is taken as the best  
 available approximation [13]. Nevertheless, the decreasing magnetic moments  
 between  $WO_2$  and  $WO_3$  are commensurate with magnetic susceptibility experi-  
 195 ments performed on these phases [40]. Henceforth, any discussion regarding the  
 perfect crystals of these phases refers to those in their magnetic ground states  
 described here.

As discussed above, semi-local functionals typically underestimate the band  
 gaps in insulating materials. This is evident in Figure 3 where, for  $WO_3$ , the  
 200 band gap is shown to be about 1.34 eV. This is almost half of experimentally  
 observed values, which lie in the range 2.6 to 2.8 eV. Varying the  $U$  parameter  
 between  $U = 0$  eV and  $U = 6$  eV has a marginal effect on the size of the band

gap in  $\text{WO}_3$ , as shown in Figure 5; an increase in the  $U$  parameter from 0 to 5.13 eV raised the band gap by approximately 0.2 eV. However, using the hybrid HSE06 functional, the band gap is predicted to be  $E_g = 2.53$  eV, which closely matches previous hybrid DFT studies on  $\text{WO}_3$  (2.56 eV)[25] as well as experimental values [32].

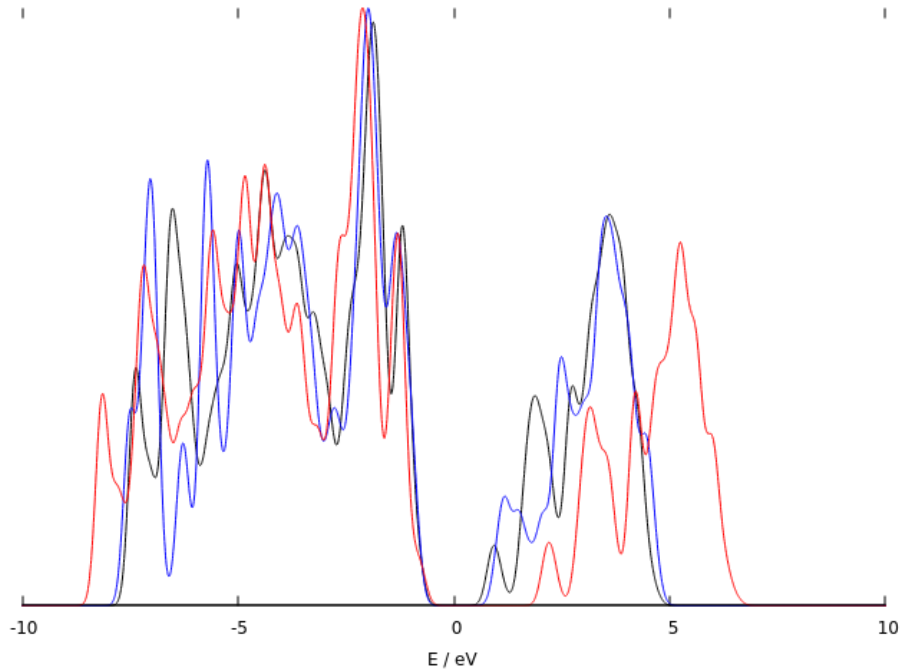


Figure 5: Total density of states for monoclinic  $\text{WO}_3$ , calculated with a  $U$  parameter of 0 eV (blue line) and 5.13 eV (solid line). The total density of states as calculated using the HSE06 hybrid functional is shown in red.

### 3.3. Oxygen vacancy defect formation energies

The oxygen vacancy formation energies for  $\text{WO}_3$  as a function of the Fermi level are presented in Figure 6 (note the plot is presented up to the band gap predicted using the HSE06 functional). In each plot, the black line denotes the vacancy formation energy of the  $V_{\text{O}(1)}$  defect, the blue line the  $V_{\text{O}(2)}$  and the red line the  $V_{\text{O}(3)}$  defect. The positions of these defects are shown in Figure 1.

The overall trend is as would be expected for a typical oxygen vacancy, with  
215 the  $V_{\text{O}}^{+2}$  defect dominant at the valence band maximum and a transition to  
the  $V_{\text{O}}^0$  defect just past the midgap. On first inspection this may appear to  
contrast with the results of Linderälv, where the transition appears much closer  
to the conduction band, however, this is due to the choice of bandgap. In this  
work the  $x$ -axis extends to the HSE06 bandgap of 2.53 eV, while Linderälv only  
220 considers up to 1.7 eV, which is the bandgap from the PBE functional, when  
plotted on the same axis, the results look similar. A more detailed comparison  
of the formation energies is presented in Table 4.

This work and that of Linderälv adopted different approaches to account  
for finite size effects, and so the comparison of the charged defects in  $\text{WO}_3$   
225 is complex. Therefore, the charge-neutral defects are considered first. Under  
oxygen-rich conditions, the formation energies calculated in this study are be-  
tween 3.11 and 3.22 eV compared to Linderälv's values of 3.34-3.44 eV with  
a discrepancy on the order of 0.2 eV. This small discrepancy may arise due  
to the chemical potentials or the choice of the exchange-correlation functional  
230 (here the PBE was used, whereas Linderälv employed the vdW-DF-CX func-  
tional). It should be noted that the difference in the formation energies for  
the defects under oxygen-rich and poor conditions are also very similar with  
2.47 eV determined here compared to 2.67 eV from Linderälv. In the Linderälv  
study the  $V_{\text{O}2}$  defect was predicted to have the lowest formation energy and  
235 a similar trend is observed here. This study suggests that there is a small  
energy difference between the oxygen vacancy on the O1 and O3 sites, while  
Linderälv predicts them to have the same energy. As the charge state of the  
defect increases the discrepancy between the the results determined here and  
Linderälv increases, with differences of  $\sim 0.5$  eV and  $\sim 0.75$  eV for the +1 and  
240 +2 charge states respectively. This may be a result of the different correction  
methods used to address the finite-size effects. Both techniques employ a point  
charge correction that considers the dielectric properties of the host material.  
There are significant differences between the dielectric tensors determined for  
 $\text{WO}_3$  here and that predicted by Linderälv, which may explain the discrepancy.

Table 4: Table showing the defect formation energies for the oxygen vacancy defects in  $\text{WO}_2$  and  $\text{WO}_3$ . Note that for  $\text{WO}_3$  all defect energies are quoted at the valence band maximum. For the O-rich case, the chemical potential for the oxygen is given as half the energy for the dimer and for the O-poor case it is determined from the oxide and the metal. The studies of Chatten *et al.* [41] and Lambert-Mauriat *et al.* [28] only quote values under O-rich conditions.

Oxide	Defect	Charge	This work		Linderälv [42]		Chatten [41]		Lambert-Mauriat [28]	
			O-rich	O-poor	O-rich	O-poor	O-rich	O-poor	O-rich	O-rich
$\text{WO}_3$	VO1	0	3.2177	0.75	3.44	0.77	4.53	3.52		
	VO2	0	3.1129	0.6452	3.34	0.67	4.41	3.06		
	VO3	0	3.2791	0.8114	3.44	0.77	3.46	2.87		
	VO1	1	1.177	-1.2907	1.68	-0.99	-	-		
	VO2	1	1.025	-1.4427	1.48	-1.19	-	-		
	VO3	1	1.139	-1.3287	1.68	-0.99	-	-		
	VO1	2	-0.759	-3.2267	-0.02	-2.65	-	-		
	VO2	2	-0.9493	-3.417	-0.22	-2.85	-	-		
	VO3	2	-0.835	-3.3027	-0.02	-2.65	-	-		
$\text{WO}_2$	VO1	0	5.4774	4.5562	2.98	2.48	-	-		
	VO2	0	4.3785	3.4586	3.54	3.04	-	-		

245 Ultimately, however, the overall agreement with the work of Linderälv is good  
for the defects in  $\text{WO}_3$ . Several other studies have also calculated formation  
energies for the charge-neutral oxygen vacancy. Both Chatten *et al.* [41] and  
Lambert-Mauriat *et al.* [28] predict an ordering of  $\text{VO3} < \text{VO2} < \text{VO1}$  for the  
thermodynamic stability of the oxygen vacancy defects, which disagrees with  
250 both the ordering predicted here and that of Linderälv [42]. It should be noted  
these works used relatively small supercells, however, the values are in the same  
range. Further, values of 3.72 and 5.3 eV have been presented by Trioni *et al.*  
*et al.* [43] and Wang *et al.* [29], however, they do not quote which site they had  
simulated. This final value from Wang *et al.* is an outlier, however, it should  
255 be noted that it is the only simulation to employ a hybrid functional.

$\text{WO}_2$  is metallic, therefore, only the neutral charge state is considered for  
the two unique oxygen vacancy sites, labelled 1 and 2 in Figure 1. The values  
calculated for the oxygen vacancy formation energies in  $\text{WO}_2$  are summarised in  
Table 4, clearly showing the wide range of formation energies and the effect of  
260 the chemical potential of oxygen. In the oxygen-poor limit, the values presented  
here agree with those proposed by Huang *et al.* (2.49 eV), who calculated the  
chemical potential of oxygen in the manner described here with a  $U$  parameter  
of 6.2 eV [44]. By contrast, the values presented in this work are considerably  
higher in the oxygen-rich limit than those proposed by Linderälv (3.54 eV and  
265 2.98 eV respectively). This is not likely due to the choice of chemical potential  
as these appear to be relatively similar based on the  $\text{WO}_3$  results. The difference  
between the oxygen-rich and poor regimes have been reduced to  $\sim 1.05$  eV here  
and 0.5 eV for Linderälv. In addition to the energies being distinctly different,  
the ordering of the sites is also different. This may be a labelling issue as it is  
270 difficult to identify sites from the images presented in this previous study.

The Magnéli phases  $\text{W}_{18}\text{O}_{49}$  and  $\text{W}_{25}\text{O}_{73}$  are vastly more complicated than  
those of  $\text{WO}_2$  and  $\text{WO}_3$ . These phases have 25 and 147 unique oxygen vacancy  
sites respectively. Therefore, we present the oxygen vacancy formation energies  
in the oxygen-rich limit in Figure 7. The highest values of the vacancy formation  
275 energies occur in regions of the unit cell, which are comprised of  $\text{WO}_2$ -like motifs,

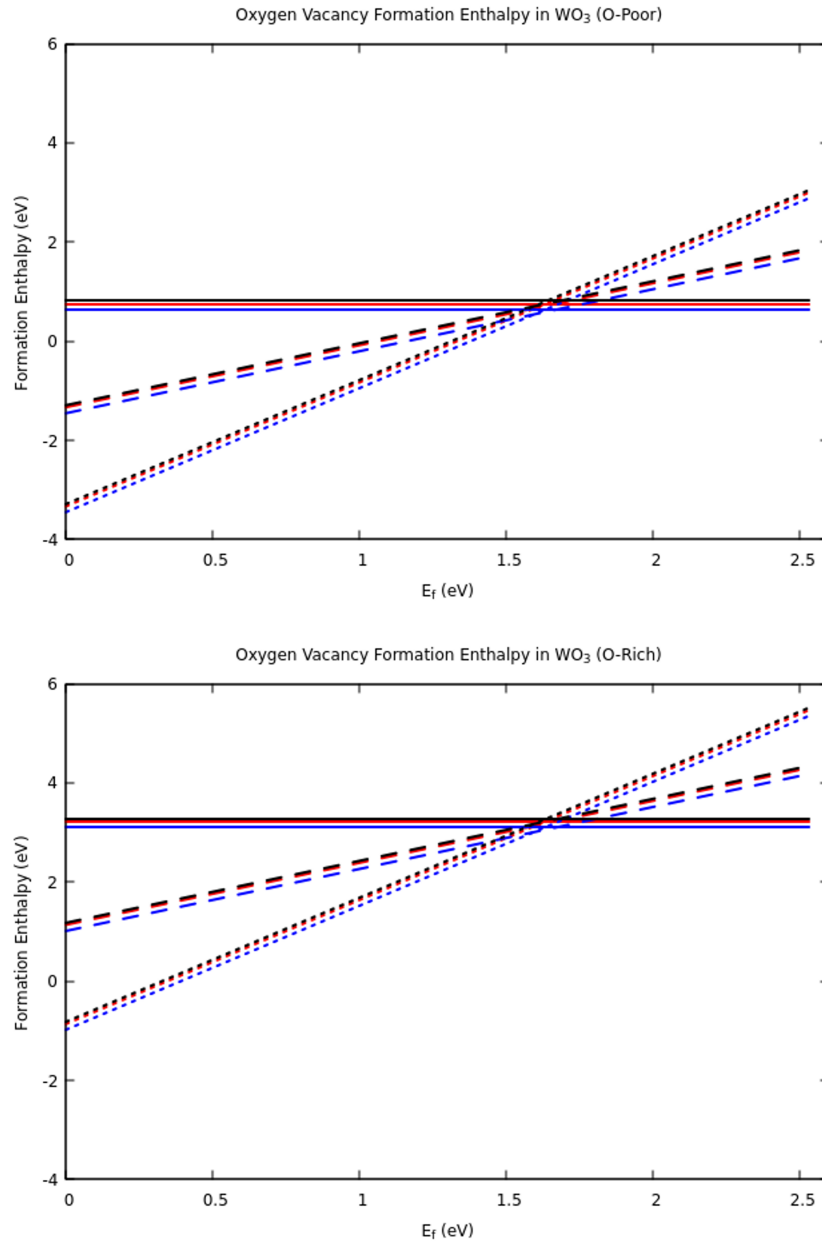
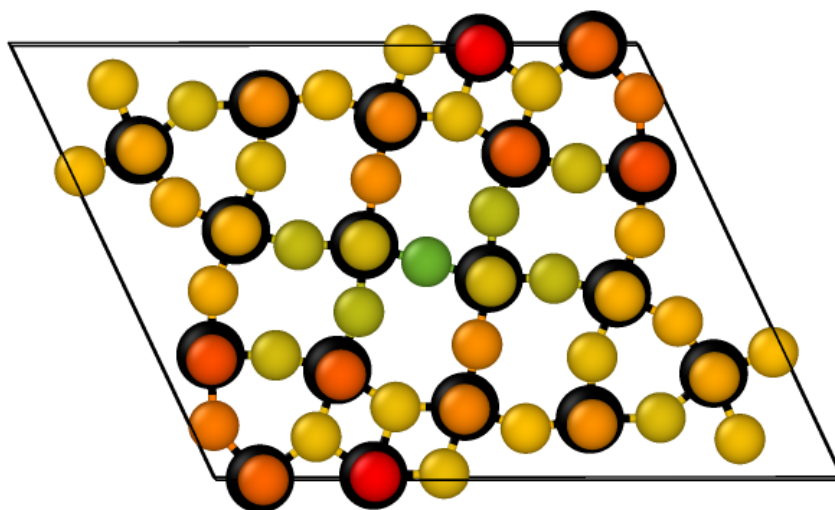


Figure 6: Oxygen vacancy formation energy in tungsten trioxide as a function of the Fermi level in both the O-rich and O-poor limits. The solid line denotes the +0 charge state, the dashed line denotes the +1 charge state, and the dotted line denotes the +2 charge state. The valence band maximum lies at 0 eV, whilst the conduction band maximum begins at 2.53 eV. The blue line the  $V_{O(2)}$  and the red line the  $V_{O(3)}$  defect.

(a)



(b)

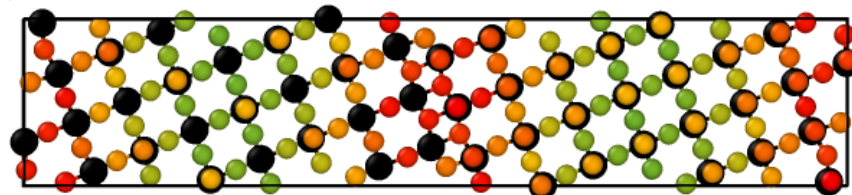


Figure 7: Oxygen vacancy formation energies in the Magnéli phases (a)  $W_{18}O_{49}$  and (b)  $W_{25}O_{73}$ . W ions in black. The formation energies are calculated in the O-rich limit.

Table 5: Oxygen vacancy migration barriers through tungsten trioxide in the +0, +1 and +2 charge states between two unique oxygen vacancy sites, i.e., A to B. Values for the reverse migration (B to A) are included in brackets.

<b>Migration barrier / eV</b>			
<b>q</b>	$V_{O(1)} \leftrightarrow V_{O(2)}$	$V_{O(1)} \leftrightarrow V_{O(3)}$	$V_{O(2)} \leftrightarrow V_{O(3)}$
<b>0</b>	0.153 (0.733)	0.765 (0.781)	0.799 (0.234)
<b>1</b>	0.222 (0.750)	0.665 (0.664)	0.791 (0.262)
<b>2</b>	0.126 (0.741)	0.726 (0.741)	0.780 (0.161)

Table 6: Oxygen vacancy migration barriers through tungsten dioxide. As there are only two unique oxygen vacancy sites, the migration barrier between two identical, adjacent vacancy sites has also been included.

<b>Migration Barrier / eV</b>		
<b>q</b>	$V_{O(1)} \leftrightarrow V_{O(2)}$	$V_{O(1)} \leftrightarrow V_{O(1)}$
<b>0</b>	1.81 (2.90)	3.12 (3.12)

whereby each oxygen atom is coordinated to three tungsten atoms. Oxygen vacancy formation energies in these regions are as high as 6.57 eV in  $W_{18}O_{49}$ . On the other hand, the lowest oxygen vacancy formation energy is found in the center of the unit cell, bridging two  $WO_6$  octahedra, with a value of 3.55 eV.

280 For both  $W_{18}O_{49}$  and  $W_{25}O_{73}$ , in the regions where the oxygen vacancy formation energy is higher, oxygen is coordinated to three tungsten atoms with a bond length of between 1.98 and 2.09 Å. This is comparable to the W-O bond lengths predicted in  $WO_2$ , which are around 2.08 Å. Lower oxygen vacancy formation energies are found in regions where oxygen is coordinated to only two  
285 tungsten atoms (as in  $WO_3$ ), where shorter bond lengths of between 1.84 and 1.97 Å are observed. Again, this is comparable to the W-O bond lengths predicted in  $WO_3$ , which are around 1.94 Å. From these observations, the Magnéli phases appear to be composed of  $WO_3$ -like and  $WO_2$ -like regions, both in terms of physical and electronic structure.

290 *3.4. Oxygen Vacancy Migration Barriers*

Finally, we present the migration barriers between oxygen vacancy sites in  $\text{WO}_3$  and  $\text{WO}_2$ . The values calculated for the neutral ( $q = 0$ ) system closely correspond to existing data reported by Le *et al.*, who reported migration barriers of  $\approx 0.14$  eV for the  $V_{\text{O}(1)} \rightarrow V_{\text{O}(2)}$  pathway and values between  $0.87 \approx$   
295  $1.07$  eV for the  $V_{\text{O}(1)} \leftrightarrow V_{\text{O}(3)}$  pathway [45]. Therefore, the accuracy of the one-image NEB calculations employed in this work is considered sufficient.

As shown in Table 5, the migration barrier required to migrate the  $V_{\text{O}(1)}$  vacancy to  $V_{\text{O}(2)}$  vacancy, and from  $V_{\text{O}(3)}$  to  $V_{\text{O}(2)}$ , are considerably smaller than the energy required to move between vacancies  $V_{\text{O}(1)}$  and  $V_{\text{O}(3)}$ . This  
300 corresponds to a preference for oxygen moving along the  $a$ -axis. Furthermore, the  $q = +1$  system exhibits noticeably different migration energies to the  $q = 0$  and  $q = +2$  systems, likely due to the unpaired electron present in this system. The anisotropy in the migration energies suggests that the orientation of  $\text{WO}_3$  may impact the rate at which the oxide interface grows into tungsten, aligning  
305 with the orientation dependency observed by Schlueter *et al.* [5].

In  $\text{WO}_2$ , the barrier for oxygen diffusion is strongly directional. The migration barrier required to migrate the  $V_{\text{O}(1)}$  vacancy to the  $V_{\text{O}(2)}$  vacancy is 1.81 eV, whilst migration in the reverse direction has a barrier of 2.90 eV. Similar values were obtained by Huang *et al.*, in which the migration barriers were 1.86  
310 eV and 2.19 eV respectively [44]. Linderalv predicted barriers of  $\sim 2.5$  and 3 eV to move between the O1 and O2 sites and back again [42]. These barriers are on the same scale as those predicted here even if there are significant discrepancies in the formation energies.

The significantly larger migration barriers mean that  $\text{WO}_2$  is far less permeable to oxygen compared to  $\text{WO}_3$ , indicating that  $\text{WO}_2$  and  $\text{WO}_2$ -like regions in the Magneli phases protect the pure tungsten metal from further oxidation. This  
315 protective behaviour has been observed experimentally and attributed broadly, but not unanimously, to  $\text{WO}_2$  or the Magneli phases [6, 46, 47]. The overall rate of diffusion of oxygen through the oxide will depend on the isotropies in the activation energies determined here, the orientation of the oxide on the surface  
320

and the magnitude of the driving force across the oxide layer.

#### 4. Conclusion

In this work, we have reviewed the physical structure of the key tungsten oxide phases observed during the oxidation of tungsten. As the tungsten-oxygen ratio evolves, from  $\text{WO}_2$  through to  $\text{WO}_3$ , we see a corresponding evolution of the electronic density of states for each phase. The W  $5d$  states that lie just below the Fermi level in  $\text{WO}_2$  shift to higher energies as the oxygen content increases, until they rise above the Fermi level in  $\text{WO}_3$ , which becomes an insulator.

By investigating the evolution of the electronic structure, the bond lengths in the  $\text{WO}_2$  and  $\text{WO}_3$  phases, and the oxygen vacancy formation energies of the four tungsten-oxygen systems of interest, we show that the substoichiometric phases,  $\text{W}_{18}\text{O}_{49}$  and  $\text{W}_{25}\text{O}_{73}$ , can be considered to be made of regions displaying  $\text{WO}_2$ -like and  $\text{WO}_3$ -like properties (namely, bond lengths and oxygen vacancy formation energies). It is suggested that the oxygen diffusion migration barriers may exhibit similar trends. This would account for the orientation dependence of the oxidation of tungsten, as well as the observation that the Magnéli phases only form thin, transient layers between  $\text{WO}_2$  and  $\text{WO}_3$ . It has been shown that the migration barriers for oxygen diffusion in  $\text{WO}_2$  are much larger than those observed in  $\text{WO}_3$  (1.81  $\sim$  2.90 eV vs. 0.15  $\sim$  0.80 eV respectively). Furthermore, it is shown that oxygen migration in the  $\langle 100 \rangle$  direction is strongly preferred in  $\text{WO}_3$ , with migration barriers as little as 0.13 eV in the +2 charge state. Therefore, if the Magnéli phases are orientated such that their  $a$ -axis lies perpendicular to the oxide-air interface, rapid diffusion of oxygen would be expected through through the  $\text{WO}_3$ -like regions. However, should they be orientated such that their  $\text{WO}_2$ -like regions occlude the  $\text{WO}_3$ -like regions from the oxide-air interface, then diffusion of oxygen through the  $b$ - or  $c$ -axes would be much slower. In this way, the orientation dependence of the system and the effect of the formation of columnar  $\text{W}_{25}\text{O}_{73}$  on the oxidation of tungsten arises

350 out of the oxygen vacancy formation energies and diffusion barriers.

## 5. Acknowledgements

Via our membership of the UK's HEC Materials Chemistry Consortium, which is funded by EPSRC (EP/R029431), this work used the ARCHER2 UK National Supercomputing Service (<http://www.archer2.ac.uk>). This work was  
355 also part-funded by the EPSRC Energy Programme (grant number EP/W006839/1). We wish to acknowledge the use of the EPSRC funded Physical Sciences Data-science Service hosted by the University of Southampton and STFC under grant number EP/S020357/1. This work was also supported by the EPSRC-funded Centre for Doctoral Training in GREEN (Growing skills for Reliable Economic  
360 Energy from Nuclear) (Grant code: EP/S022295/1).

## References

- [1] D. Stork, et al., Materials R&D for a timely DEMO: Key findings and recommendations of the eu roadmap materials assessment group, *Fusion Engineering and Design* 89 (7) (2014) 1586–1594.
- 365 [2] D. Adomavicius, M. Lisak, A conceptual study of commercial fusion power plants, EFDA – RP – RE – 5.0, 2005.
- [3] F. Maekawa, M. Wada, C. Konno, Y. Kasugai, Y. Ikeda, Decay heat experiment featuring low-energy neutron induced tungsten-187 production in ITER baffle plates and its analysis, *Fusion Engineering and Design* 51-52  
370 (2000) 809–814.
- [4] M. Togaru, et al., Direct observation of tungsten oxidation studied by *in situ* environmental TEM, *Materials Characterization* 174 (2021) 111016.
- [5] K. Schlueter, M. Balden, Dependence of oxidation on the surface orientation of tungsten grains, *International Journal of Refractory Metals and Hard Materials* 79 (2019) 102–107.  
375

- [6] S. Cifuentes, M. Monge, P. Pérez, On the oxidation mechanism of pure tungsten in the temperature range 600–800°C, *Corrosion Science* 57 (2012) 114–121.
- [7] A. Atkinson, Wagner theory and short circuit diffusion, *Materials Science and Technology* 4 (12) (1988) 1046–1051.
- [8] E. Indrea, E. Bica, E.-J. Popovici, R.-C. Suci, M.-C. Rosu, D. Silipas, Rietveld refinement of powder X-ray diffraction of nanocrystalline noble metals - tungsten trioxide, *Revue Roumaine de Chimie* 56 (2011) 589–593.
- [9] T. Vogt, P. M. Woodward, B. A. Hunter, The high-temperature phases of  $\text{WO}_3$ , *Journal of Solid State Chemistry* 144 (1) (1999) 209–215.
- [10] V. L. Shaposhnikov, D. B. Migas, V. N. Rodin, V. E. Borisenko, Ab initio investigation of structural and electronic properties of tungsten dioxide, *Physica Status Solidi (b)* 248 (6) (2011) 1471–1476.
- [11] R. Diehl, G. Brandt, E. Salje, The crystal structure of triclinic  $\text{WO}_3$ , *Acta Crystallographica Section B* 34 (4) (1978) 1105–1111.
- [12] W. L. Kehl, R. G. Hay, D. Wahl, The structure of tetragonal tungsten trioxide, *Journal of Applied Physics* 23 (2) (1952) 212–215.
- [13] E. Salje, The orthorhombic phase of  $\text{WO}_3$ , *Acta Crystallographica Section B* 33 (2) (1977) 574–577.
- [14] K. Viswanathan, K. Brandt, E. Salje, Crystal structure and charge carrier concentration of  $\text{W}_{18}\text{O}_{49}$ , *Journal of Solid State Chemistry* 36 (1) (1981) 45–51.
- [15] M. Sundberg, The crystal and defect structures of  $\text{W}_{25}\text{O}_{73}$ , a member of the homologous series  $\text{W}_n\text{O}_{3n-2}$ , *Acta Crystallographica Section B* 32 (7) (1976) 2144–2149.
- [16] G. Kresse, J. Hafner, Ab initio molecular dynamics for liquid metals, *Physical Review B* 47 (1993) 558–561.

- [17] G. Kresse, J. Furthmüller, Efficiency of ab-initio total energy calculations for metals and semiconductors using a plane-wave basis set, Computational Materials Science 6 (1) (1996) 15–50.
- [18] G. Kresse, J. Furthmüller, Efficient iterative schemes for ab initio total-energy calculations using a plane-wave basis set, Physical Review B 54 (1996) 11169–11186.
- [19] G. Kresse, D. Joubert, From ultrasoft pseudopotentials to the projector augmented-wave method, Physical Review B 59 (1999) 1758–1775.
- [20] S. L. Dudarev, G. A. Botton, S. Y. Savrasov, C. J. Humphreys, A. P. Sutton, Electron-energy-loss spectra and the structural stability of nickel oxide: An LSDA + U study, Physical Review B 57 (1998) 1505–1509.
- [21] M. Cococcioni, S. de Gironcoli, Linear response approach to the calculation of the effective interaction parameters in the LDA + U method, Physical Review B 71 (2005) 035105.
- [22] Y. Kumagai, F. Oba, Electrostatics-based finite-size corrections for first-principles point defect calculations, Physical Review B 89 (2014) 195205.
- [23] J. P. Perdew, K. Burke, M. Ernzerhof, Generalized gradient approximation made simple, Phys. Rev. Lett. 77 (1996) 3865–3868.
- [24] B. Uberuaga, H. Jonsson, A climbing image nudged elastic band method for finding saddle points and minimum energy paths, J. Chem. Phys. 113 (2000) 9901–9904.
- [25] W. Wang, A. Janotti, C. G. Van de Walle, Role of oxygen vacancies in crystalline  $\text{WO}_3$ , J. Mater. Chem. C 4 (2016) 6641–6648.
- [26] A. Jain, et al., Commentary: The materials project: A materials genome approach to accelerating materials innovation, APL Materials 1 (1) (2013) 011002.

- [27] T. A. Shuaibu, H. Isah, Density functional theory analysis on the structural properties of cubic and monoclinic tungsten trioxide, International Journal of Science for Global Sustainability 5 (2) (2019) 150.
- [28] C. Lambert-Mauriat, V. Oison, Density-functional study of oxygen vacancies in monoclinic tungsten oxide, Journal of Physics: Condensed Matter 18 (31) (2006) 7361.
- [29] F. Wang, C. Di Valentin, G. Pacchioni, Semiconductor-to-metal transition in  $\text{WO}_{3-x}$ : Nature of the oxygen vacancy, Phys. Rev. B 84 (2011) 073103.
- [30] S. Tanisaki, Crystal structure of monoclinic tungsten trioxide at room temperature, Journal of the Physical Society of Japan 15 (1960) 573–581.
- [31] R. J. Sáenz-Hernández, et al., Correlation between thickness and optical properties in nanocrystalline  $\gamma$ -monoclinic  $\text{WO}_3$  thin films, Coatings 12 (11).
- [32] B. O. Loopstra, H. M. Rietveld, Further refinement of the structure of  $\text{WO}_3$ , Acta Crystallographica Section B 25 (7) (1969) 1420–1421.
- [33] A. A. Bolzan, B. J. Kennedy, C. J. Howard, Neutron powder diffraction study of molybdenum and tungsten dioxides, Australian Journal of Chemistry 48 (1995) 1473–1477.
- [34] H. Xiao, J. Tahir-Kheli, W. A. Goddard III, Accurate band gaps for semiconductors from density functional theory, The Journal of Physical Chemistry Letters 2 (3) (2011) 212–217.
- [35] J. Paier, M. Marsman, G. Kresse, Why does the B3LYP hybrid functional fail for metals?, The Journal of Chemical Physics 127 (2) (2007) 024103.
- [36] A. A. Yaremchenko, D. D. Khalyavin, M. V. Patrakeev, Uncertainty of oxygen content in highly nonstoichiometric oxides from neutron diffraction data: example of perovskite-type  $\text{Ba}_{0.5}\text{Sr}_{0.5}\text{Co}_{0.8}\text{Fe}_{0.2}\text{O}_3$ , J. Mater. Chem. A 5 (2017) 3456–3463.

- [37] J. A. Kaduk, Chemical reasonableness in rietveld analysis: *Inorganics, Powder Diffraction* 22 (3) (2007) 268–278.
- [38] B. S. J. P. Tian, Testing different methods for estimating uncertainties on rietveld refined parameters using sr rietveld 226 (12).
- 460 [39] W. Liu, P. Jiang, Y. Xiao, J. Liu, A study of the hydrogen adsorption mechanism of  $W_{18}O_{49}$  using first-principles calculations, *Computational Materials Science* 154 (2018) 53–59.
- [40] M. J. Sienko, B. Banerjee, Studies in non-stoichiometry: Magnetic susceptibilities in the tungsten-oxygen system1, *Journal of the American Chemical Society* 83 (20) (1961) 4149–4152.
- 465 [41] R. Chatten, A. V. Chadwick, A. Rougier, P. J. D. Lindan, The oxygen vacancy in crystal phases of  $WO_3$ , *The Journal of Physical Chemistry B* 109 (8) (2005) 3146–3156.
- [42] C. Linderälv, Structural and thermodynamical properties of tungsten oxides from first-principles calculations, Chalmers University of Technology (2016).
- 470 [43] M. I. Trioni, F. Cargnoni, S. Americo, R. Soave, New insight into the electronic and magnetic properties of sub-stoichiometric  $WO_3$ : A theoretical perspective, *Crystals* 14 (4).
- [44] S. Huang, R. Kerr, S. Murphy, M. R. Gilbert, J. Marian, Multilayer interface tracking model of pure tungsten oxidation, *Modelling and Simulation in Materials Science and Engineering* 30 (8) (2022) 085015.
- 475 [45] H. Le, v. Nam, T. Phan, Migrations of oxygen vacancy in tungsten oxide ( $WO_3$ ): A density functional theory study, *Computational Materials Science* 90 (2014) 171–176.
- 480 [46] E. A. Kellett, S. E. Rogers, The structure of oxide layers on tungsten, *Journal of The Electrochemical Society* 110 (6) (1963) 502.

- [47] J. Habainy, S. Iyengar, K. B. Surreddi, Y. Lee, Y. Dai, Formation of oxide layers on tungsten at low oxygen partial pressures, *Journal of Nuclear Materials* 506 (2018) 26–34.

485